INORGANIC CHEMISTRY FRONTIERS

RESEARCH ARTICLE

View Article Online
View Journal | View Issue

Cite this: *Inorg. Chem. Front.*, 2023, **10**, 78

The synthesis of zeolitic imidazolate framework/prussian blue analogue heterostructure composites and their application in supercapacitors†

Xinyue Wu,[a] Qingling Jing,[a] Fancheng Sun[a,b] and Huan Pang *[a]

Received 12th September 2022,
Accepted 8th November 2022

DOI: 10.1039/d2qi01966c

rsc.li/frontiers-inorganic

Zeolitic imidazolate frameworks (ZIFs) and Prussian blue analogues (PBAs) are regarded as a subfamily of MOFs and possess great electrochemical characteristics, which are widely employed in energy and environmental applications. Benefiting from the merits of these two MOFs, we report a simple ion-exchange method to prepare ZIF-67/PBA heterostructure composites (abbreviated as ZP composites) with ZIF-67 and PBA as precursors. After low-temperature calcination, the structure converted into bimetallic N-doped dodecahedra that retained the structures of the ZP composites. The as-prepared ZP composites were utilized as electrode materials for supercapacitors that exhibited great rate capability and cycling stability. Furthermore, we assembled an asymmetric supercapacitor device with ZP composites and activated carbon. These results demonstrated that dual-MOF heterostructure composites showed great potential when applied as electrode materials.

Introduction

Metal–organic frameworks (MOFs) have attracted widespread attention in environmental and energy applications owing to their controllable pore sizes, large specific surface area and crystalline porous structure, and are composed of metal ions and organic linkers.[1–6] However, MOFs suffer from inferior electrical conductivity and unsatisfactory chemical stability, limiting the further development of MOFs.[7,8] To overcome these shortcomings, great efforts have been devoted to designing and deriving MOF precursors to explore more advanced nanomaterials with chemical compositions and controlled architectures.[9] The synthesis of desirable functional materials for the construction of complex MOF composites is highly promising.[10–13]

With the increasing demand for efficient energy storage systems, efforts to develop supercapacitors (SCs) with excellent cycling stability, fast charge–discharge processes, and superior power density.[14] Various MOFs are regarded as remarkable potential electrode materials used in SCs due to their low cost and high activity.[15–18] Some optimization strategies have been explored to improve the electrochemical performance of the MOFs, such as the combination with conductive materials, the doping of the metal and non-metal, and the construction of the hollow structure.[19–22] Impressively, dual-MOF heterostructure composites efficiently integrating two MOFs have attracted considerable attention, owing to their desirable functionality and controllable structures.[23,24] This integration was usually prepared through the growth guest MOFs on pre-synthesized host MOFs or growth kinetic controlled routes by various chemical interactions, including epitaxial growth, surfactant assisted growth, ligand/metal ion exchange and so on.[25,26] To date, heterostructure composites have various architectures such as core–shell, core–satellite, hollow multi-shell, and asymmetric structures, which resulted from the combination of different functional materials.[27,28] The complex structure of dual-MOF heterostructure composites not only showed structural diversity, but also had considerable potential in practical applications when compared with those of original MOF materials, especially in energy storage. In particular, as a subfamily of MOFs, zeolitic imidazolate frameworks (ZIFs) and Prussian blue analogues (PBAs) with their great electrochemical characteristics are applied in catalysis, adsorption, sensors, energy conversion and storage.[29,30] ZIFs with excellent chemical and thermal stability consist of transition metal centres (Co, Cu, Zn, *etc.*) and imidazole ligands, generating their expanded zeolite topologies.[31,32] PBAs possess a three dimensional (3D) open-framework, adjustable composition, and controllable structure with the transition metal

[a]*School of Chemistry and Chemical Engineering, Yangzhou University, Yangzhou, 225009 Jiangsu, P. R. China. E-mail: huanpangchem@hotmail.com, panghuan@yzu.edu.cn*
[b]*Interdisciplinary Materials Research Center, Institute for Advanced Study, Chengdu University, Chengdu, 610106 Sichuan, P.R. China*
† Electronic supplementary information (ESI) available. See DOI: https://doi.org/10.1039/d2qi01966c

centres surrounded by six cyanide groups (C≡N).[33,34] Benefiting from the merits of the two MOFs, the combination of the ZIF and PBA can be an effective method to enhance the electrochemical performance and make up for the problem of low specific capacitance when each is used as an electrode material.

Hence, we report a simple method to prepare a series of ZIF-67/PBA heterostructure composites (abbreviated as ZP composites) with ZIF-67 nanoparticles as host MOFs by the ion-exchange method. Furthermore, after low-temperature calcination, the ZP composites converted into bimetallic N-doped dodecahedra that retained the structures of the ZP composites, generating final products denoted as ZP-*X* (*X* represents temperature). Specifically, the as-prepared ZP2-250 materials exhibited great electrochemical performances and a specific capacitance of 190.7 F g^{-1} at 0.5 A g^{-1} in a 3.0 M KOH solution. Besides, the aqueous asymmetric supercapacitor (ASC) device was assembled and it exhibited good electrochemical performance. This synthetic strategy can be extended to the synthesis of other dual-MOF heterostructure composites to further develop various electrochemical applications.

Results and discussion

ZP composites were synthesized through an ion change method by changing the water/ethanol ratio (Scheme 1). The ZIF-67 nanoparticles and potassium ferricyanide ($K_3[Fe(CN)_6]$) were dispersed in ethanol and water mixed solution with the volume ratios of ethanol and water = 9 : 1, 1 : 1, and 1 : 2.[35] After stirring at room temperature for 4 h, the colour of the solution changes from bright purple to deep purple. A series of ZP composites were attained, denoted as ZP1 (ethanol : water = 9 : 1), ZP2 (ethanol : water = 1 : 1), and ZP3 (ethanol : water = 1 : 2), respectively. The scanning electron microscopy (SEM) images in Fig. 1a–f revealed that ZP composites basically retained the original rhombic dodecahedron shape with an average size of around 1100 nm. The $[Fe(CN)_6]^{3-}$ anions react with the Co^{2+} cations that are released from ZIF-67 nanoparticles, forming a PBA shell. The surfaces of the ZP composites changed from smooth to rough with the increase of water in the mixed solution, generating continuous PBA nanocubes on the surface of ZP2. The nanosheets began to grow when the volume ratio of ethanol and water = 1 : 2 because ZIF-67 was unstable and hydrolyzed in an aqueous solution. Transmission electron microscopy (TEM) measurements can

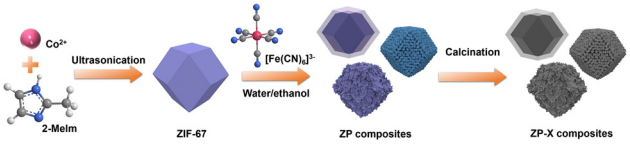

Scheme 1 A simple route for the synthesis of ZIF-67/PBA composites and derivatives.

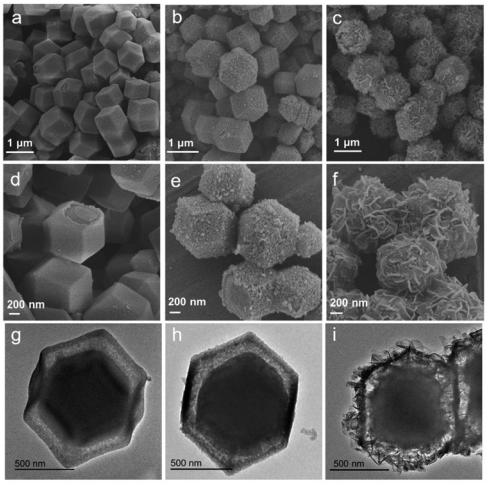

Fig. 1 The SEM images of (a, d) ZP1, (b, e) ZP2, and (c, f) ZP3 composites. (g–i) The TEM images of ZP1, ZP2, and ZP3 composites.

observe that ZP composites have formed a yolk–shell with a thin shell and a thick core (Fig. 1g–i).

Depending on the results of thermogravimetric analysis (TGA) (Fig. S1†), the ZP2 composites can be stable up to 400 °C under a N_2 atmosphere before decomposition of the framework structure, which involved the removal of the coordinated water and some organic ligands from the ZP2 composite structure. To modulate its microstructure, we calcined ZP composites at different target temperatures under a N_2 atmosphere (150, 250, 350 °C), obtaining ZP-*X* (*X* denotes temperature). Fig. 2a–c and Fig. S2† show that the original rhombic dodecahedron shape of ZP composites can be maintained after calcining at different temperatures. To illustrate the inner structure of ZP composites, the TEM images in

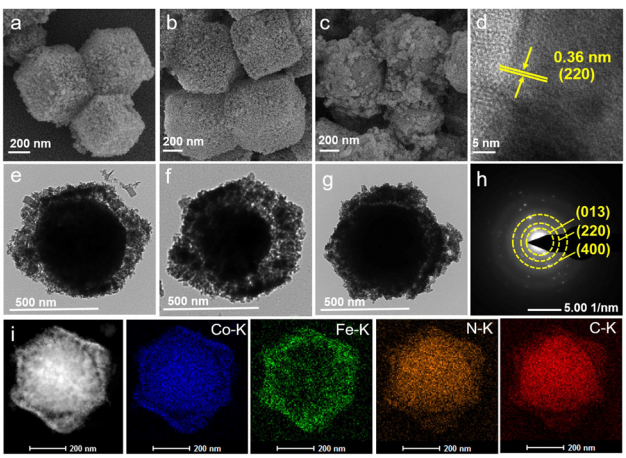

Fig. 2 (a–c) The SEM images of ZP2-150, ZP2-250, and ZP2-350 composites. (d) High-resolution TEM image of ZP2-250 composites. (e–g) The TEM images of ZP2-150, ZP2-250, and ZP2-350 composites. (h) The selected area electron diffraction (SAED) pattern of ZP2-250 composites. (i) HRTEM-EDX elemental mapping images of Co–K, Fe–K, N–K, and C–K in ZP2-250 composites.

Fig. 2e–g show that the pores on the surface became larger and denser, which could make the active sites exposed more easily. The high-resolution transmission electron microscopy (HRTEM) image (Fig. 2d) shows well-resolved lattice fringes with a *d*-spacing of 0.36 nm, which is consistent with the (220) plane of the CoFe-PBA phase. The selected area electron diffraction (SAED) pattern (Fig. 2h) exhibited separated concentric rings from the (220) and (400) facets of CoFe-PBA and (013) facets of ZIF-67. The high-angle annular dark-field scanning transmission electron microscopy (HAADF-STEM) image and elemental mapping of the ZIF-67/PBA heterostructure composites in Fig. 2i show the presence of elements Co, C, N, and O in ZIF-67 nanoparticles and the element Fe in potassium ferricyanide, further illustrating the presence and homogeneous distribution of these elements.

To further confirm the structures of all samples, the ZIF-67 nanoparticles and ZIF-67/PBA heterostructure composites have been subjected to powder X-ray diffraction (XRD) to analyse the purity and phase composition, as shown in Fig. 3a, S3 and S4.† There were no crystalline impurities observed, and the crystalline phases of the ZIF-67 nanoparticles were in agreement with those previously reported in the literature.[36] The ZIF-67/PBA heterostructure composites maintain the framework of ZIF-67, which can be observed that all diffraction peaks were in good accordance with the simulated pattern. Apart from the diffraction peaks of ZIF-67, two residual peaks of the ZP composites at 25.0° and 35.5° were identified as the (220) and (400) planes of CoFe PBA, which strongly supported the generation of ZP composites.[37] After heat treating ZP composites under a nitrogen atmosphere at low temperature, the products ZP-*X* composites essentially preserved the primary shape of the ZIF-67 crystal. Furthermore, the diffraction peaks of the composites become sharper with the increase of annealing temperature, indicating the improved crystallinity of the ZIF-67 phase. This also confirms that there is no obvious structural change during low-temperature calcination.

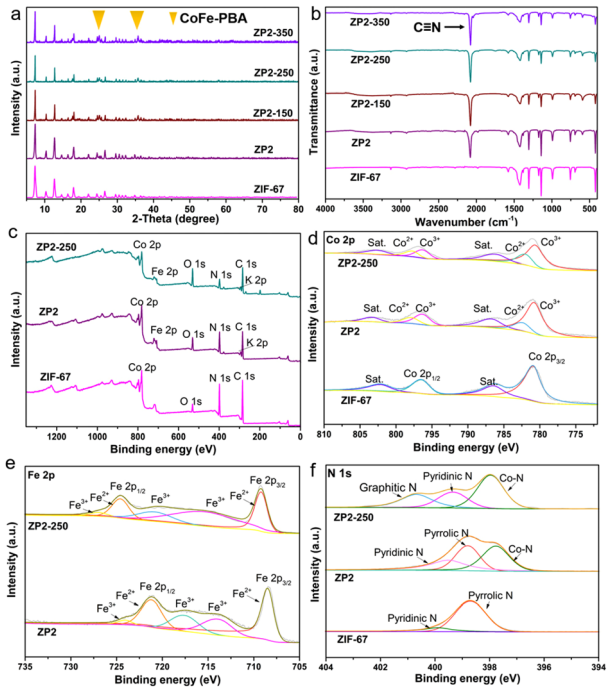

Fig. 3 (a) XRD patterns and (b) FT-IR spectra of ZIF-67, ZP2, ZP2-150, ZP2-250, and ZP2-350 composites. (c) Survey XPS spectrum of ZIF-67, ZP2, and ZP2-250 composites. (d–f) High-resolution Co 2p, Fe 2p, and N 1s XPS spectra.

The FT-IR spectra of these ZP composites (Fig. 3b, S5 and S6†) were examined to investigate the chemical bonding and chemical compositions. The vibrational modes of ZP composites were similar to that of ZIF-67, suggesting that the framework of ZIF-67 remained the same after PBA modification. Obviously, a sharp absorption peak at ≈2080 cm^{-1} can be observed in the FT-IR spectrum, which is assigned to the characteristic stretching vibration of C≡N from $[Fe(CN)_6]^{3-}$ anions.[38] The peak at 593 cm^{-1} was attributed to the generation of the M–O (M = Fe or Co) structure.[39] All the results illustrated that PBA nanoparticles have been generated, implying the successful synthesis of ZP composites. Besides, the same functional groups were reserved after the calcination activation of ZP composites at 150–350 °C. It can be inferred that low-temperature annealing is the most suitable method to improve the performance of MOF precursors.

The compositions and chemical states of the ZIF-67, ZP2 and ZP2-250 composites were investigated by XPS. The survey XPS spectrum (Fig. 3c) showed ZP2 and ZP2-250 composites containing Co 2p, Fe 2p, O 1 s, C 1 s, N 1s and K 1s. The Co 2p spectrum (Fig. 3d) has two dominant peaks of Co 2p3/2 and Co 2p1/2 accompanied by the related satellite peaks, confirming the coexistence of Co^{3+} and Co^{2+}.[35] Meanwhile, the high-resolution XPS spectrum of Fe 2p in Fig. 3e included two main peaks namely Fe 2p3/2 (708.6 eV) and Fe 2p1/2 (721.4 eV). Different from the ZIF-67 and ZP2 composites, the N 1s spectrum of the ZP2-250 composites (Fig. 3f) shows three peaks at 398.5, 400.0 and 401.1 eV corresponding to Co–N, pyrrolic N and graphitic N, which illustrated that N atoms have been successfully mixed into ZP2-250 composites. Compared with ZIF-697, ZP2 and ZP2-250 composites have a Co–N bond, meaning the N atom has been doped in ZIF/PBA heterostructures. The pyridinic N and pyrrolic N bonds are regarded as great electron donors and can improve the electron transfer rate and wettability, strongly contributing to pseudocapacitive reactions. The graphitic N bond has been found in ZP2-250 composites after calcination, which was converted from a partially unstable pyrrolic N bond. The center of graphitic N donates a free electron within the sp^2 carbon structure and can effectively improve electronic conductivity and electron transfer, thus leading to enhanced specific capacitance.[40]

A three-electrode system with Hg/HgO as the reference electrode and Pt as the counter electrode was established. The electrochemical performance of the as-prepared samples as electrode materials was investigated in a 3.0 M KOH electrolyte. Cyclic voltammetry (CV) and galvanostatic charge–discharge (GCD) tests were used to evaluate the electrochemical capacitive performances.[41,42] The typical pseudocapacitive

behaviour was proved by the pairs of redox peaks in the CV curves for these electrodes at different scanning rates and potentials (Fig. 4c, S8, S9, S11, S12, S14 and S15†). It can be seen that the redox current increased upon increasing the scan rate and the shape of the CV curve was well maintained even at a large scan rate of 100 mV s^{-1}.[43,44] Meanwhile, the oxidation and reduction peaks switched slightly toward higher and lower potentials, respectively. ZP2-250 composites displayed a higher peak current than other electrodes, suggesting that ZP2-250 composites had remarkably enhanced electrochemical activity. The shift of the reduction peak in Fig. S12† can be attributed to the change in the valence state of Co according to the Co 2p XPS spectra in Fig. 3d and Fig. S7.† The redox peaks of all samples can be observed that were ascribed to the valence state-changing processes of Co^{2+}/Co^{3+} and Fe^{2+}/Fe^{3+}, respectively. The equations of the associated faradaic redox reactions are as follows:

$$K_2Co(\text{II})Fe(\text{II})(CN)_6 + 2OH^- \rightarrow K_2Co(\text{III})Fe(\text{III})(CN)_6(OH)_2 + 2e^-$$

$$Co(\text{II})(MeIm)_2 + OH^- \rightarrow Co(\text{III})(MeIm)_2(OH) + e^-$$

The charge–discharge capacitance performance of each sample is compared in Fig. 4d, S10, S13 and S16,† which exhibited the GCD curves of the ZP and ZP-*X* electrodes at different current densities. The representative potential plateaus of the GCD curves were in good agreement with the CV curves. Apparently, the charge–discharge mechanisms of the ZP composites were associated with faradaic behaviour owing to the nonlinear behaviour of the discharge curves and voltage plateau. The corresponding specific capacitance values of ZP1, ZP2, and ZP3 (Fig. 4a) were 92.8, 114.6, and 62.2 F g^{-1} at 0.5 A g^{-1}, which were higher than that of ZIF-67 (Fig. S19†). Meanwhile, the corresponding specific capacitance values of ZP1-*X*, ZP2-*X*, and ZP3-*X* were 96.8, 76.0, 112.6, 88.4, 190.7, 117.3, 63.4, 64.7, and 73.6 F g^{-1} at 0.5 A g^{-1} (Fig. 4b), respectively. The discharging time of the ZP2-250 electrode is much longer than that of ZP2, demonstrating that the specific capacitance is highly improved by low-temperature calcination. Besides, the specific capacitance of the ZP2-250 electrode was higher than that of the other ZIF-based electrode, which was reported recently (see Table S1†). Compared with other electrodes, the ZP2-250 composites maintain approximately 80% (152.2 F g^{-1}) specific capacitance at 5.0 A g^{-1} (Fig. 4b), which exhibited superior rate capability. The cycling stability of the ZP2-250 electrode was further investigated. The specific capacitance retention of the ZP2-250 electrode was approximately 82.14% after 3000 cycles (Fig. 4e). The collapse of the ZP2-250 structure during the long cycles that repeated shuttling of OH^- at the electrode/electrolyte interface was the main reason for the reduced capacitance, as shown in Fig. S20.†[45] Electrochemical impedance spectroscopy (EIS) measurements were performed and Fig. S17 and S18† present their corresponding Nyquist plots. The slope of the straight line was a reflection of Warburg impedance in the low-frequency regions. The ZP2-250 electrodes present that the straight line along the Y axis was more ideal, indicating that the diffusion resistance was smaller. In the case of the uncalcined ZP electrodes, the sites of the PBA and the ZIF-67 unit cell were in part filled by the coordinated water content, reducing the total number of diffusion sites that are available to K^+ ions and leading to limited capacitance. The low-temperature calcination can provide a large specific surface area and increased micropore volume, which can increase the contact between the electrode and the electrolyte, supply more active sites and enhance the reactivity (Table S2†). The ZP composites' open framework began to collapse with the increase in annealing temperature. These results demonstrated that the ZP2-250 composites showed great electrochemical performance thanks to their structural stability, efficient diffusion of K^+ ions, and high specific surface area.

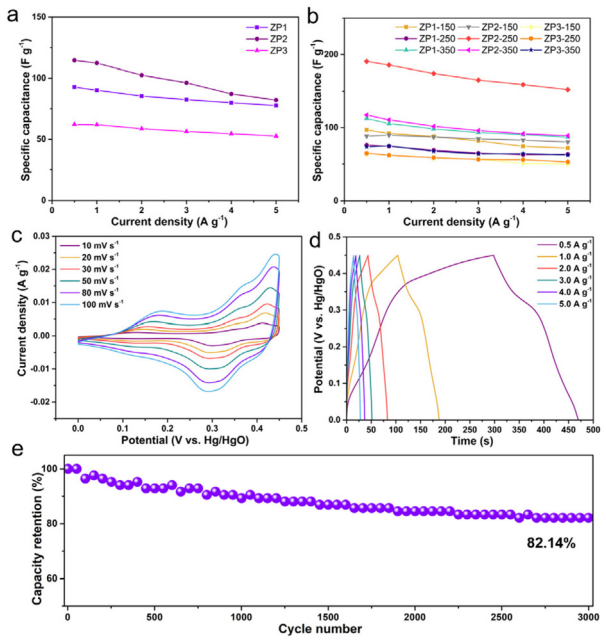

Fig. 4 (a) Specific capacitance at different current densities of ZP1, ZP2, and ZP3 composites. (b) Specific capacitance at different current densities of ZP1-*X*, ZP2-*X*, and ZP3-*X* composites. (c) CV curves of ZP2-250 composites at different scanning rates. (d) GCD curves of ZP2-250 composites at different current densities. (e) Cycling performance of ZP2-250 composites at 3.0 A g^{-1}.

Besides, an aqueous solution device ZP2-250//AC was assembled with ZP2-250 as the positive electrode and activated carbon (AC) as the negative electrode to further investigate the practical application of ZP2-250 composites. At different scanning rates and different voltages, the CV curves of ZP2-250//AC are presented in Fig. 5a and b. The ZP2-250//AC water-based device displayed pseudo-capacitance behaviour owing to the distinct oxidation and deoxidation peaks. Besides, the CV curve was well formed even at a scanning rate of 100 mV s^{-1}, illustrating the outstanding rate performance of the ZP2-250// AC aqueous solution device. The ZP2-250//AC aqueous solution device has been further researched on the charge–discharge performance. The GCD curves of this device from 0.5 to 5.0 A

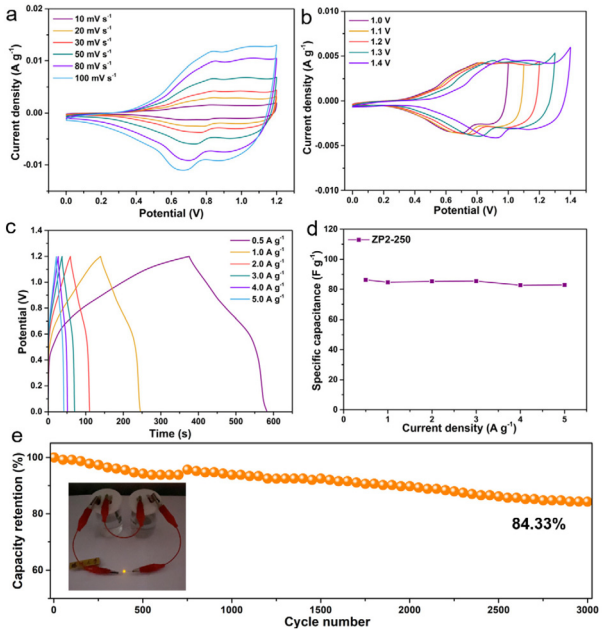

Fig. 5 Electrochemical properties of the as-prepared ZP2-250//AC device. (a) CV curves of the ZP2-250 electrode at different scanning rates. (b) CV curves of the ZP2-250 electrode at different voltages. (c) GCD curves of ZP2-250 at various current densities. (d) Specific capacitance at different current densities of ZP2-250; (e) cycling performance of ZP2-250 at 3.0 A g^{-1} (inset of (e), an optical image of two ZP2-250//AC devices linked in series to light up a blue LED).

g^{-1} are presented in Fig. 5c, and the corresponding specific capacitance values were 86.3, 84.7, 85.3, 85.5, 82.7 and 82.9 F g^{-1} (Fig. 5d). The cycling stability of the ZP2-250//AC aqueous device (Fig. 5e) was tested, which demonstrated that the capacitance retention of the ZP2-250//AC aqueous device was 84.33% after 3000 cycles at 3.0 A g^{-1}. Significantly, the inset image of Fig. 5e shows that a yellow LED has been illuminated by two ZP2-250//AC devices linked in series, which illustrated big application potential for the ZP2-250//AC aqueous device.

In short, the greater electrochemical properties of ZP-*X* composites could be attributed to the following reasons according to the electrochemical reaction mechanism: (1) an incessant conductive network has been generated by the continuous PBA nanocubes, which can efficiently enhance the spreading of OH^- between the electrolyte and the active material. (2) Micro/nanostructures are constructed with more adequate active centres and the larger specific surface area of the electrolyte, offering abundant ion and electron transport pathways and expediting electrochemical reactions. (3) Low-temperature calcination can remove coordinated water and offer extra free volume that helps buffer volume strain during repeated charging and discharging processes.

Conclusions

In summary, we report a simple synthetic route to prepare ZIF-67/PBA heterostructure composites by the ion-exchange method with the volume ratios of ethanol and water = 9 : 1, 1 : 1, and 1 : 2, which can be used as efficient electrode materials. After low-temperature calcination, the structures of the ZP composites are still retained and the electrochemical performance has improved. Specifically, the ZP2-250 composites exhibited a specific capacitance of 190.7 F g^{-1} and great cycling stability (capacitance retention ≈82.14%) in three-electrode systems. This kind of synthesis strategy can be extended to the synthesis of other dual-MOF heterostructure composites with multiple elemental components due to the characteristics of low cost, facile synthesis and environmental friendliness, which can inspire further capability for various electrochemical applications.

Conflicts of interest

There are no conflicts to declare.

Acknowledgements

This work was supported by the National Natural Science Foundation of China (U1904215), the Natural Science Foundation of Jiangsu Province (BK20200044), and the Changjiang Scholars Program of the Ministry of Education (Q2018270). The authors acknowledge the Priority Academic Program Development of Jiangsu Higher Education Institutions.

References

1 X. Xiao, L. Zou, H. Pang and Q. Xu, Synthesis of Micro/Nanoscaled Metal–Organic Frameworks and Their Direct Electrochemical Applications, *Chem. Soc. Rev.*, 2020, **49**, 301–331.
2 X. Shi, Y. Shan, M. Du and H. Pang, Synthesis and Application of Metal-Organic Framework Films, *Coord. Chem. Rev.*, 2021, **444**, 214060.
3 H. Furukawa, K. E. Cordova, M. O'Keeffe and O. M. Yaghi, The Chemistry and Applications of Metal-Organic Frameworks, *Science*, 2013, **341**, 1230444.
4 X. Chen, W. Li, G. Zhang, F. Sun, Q. Jing and H. Pang, Highly Stable and Activated Cerium-Based MOFs Superstructures for Ultrahigh Selective Uranium(VI) Capture from Simulated Seawater, *Mater. Today Chem.*, 2022, **23**, 100705.
5 F. Yang, M. Du, K. Yin, Z. Qiu, J. Zhao, C. Liu, G. Zhang, Y. Gao and H. Pang, Applications of Metal-Organic Frameworks in Water Treatment: A Review, *Small*, 2022, **18**, 2105715.
6 S. Zhao, C. Tan, C.-T. He, P. An, F. Xie, S. Jiang, Y. Zhu, K.-H. Wu, B. Zhang, H. Li, J. Zhang, Y. Chen, S. Liu, J. Dong and Z. Tang, Structural Transformation of Highly Active Metal–Organic Framework Electrocatalysts during

the Oxygen Evolution Reaction, *Nat. Energy*, 2020, **5**, 881–890.
7 Y. Peng, Y. Bai, C. Liu, S. Cao, Q. Kong and H. Pang, Applications of Metal–Organic Framework-Derived N, P, S Doped Materials in Electrochemical Energy Conversion and Storage, *Coord. Chem. Rev.*, 2022, **466**, 214602.
8 Y. Peng, J. Xu, J. Xu, J. Ma, Y. Bai, S. Cao, S. Zhang and H. Pang, Metal-Organic Framework (MOF) Composites as Promising Materials for Energy Storage Applications, *Adv. Colloid Interface Sci.*, 2022, **307**, 102732.
9 P. Xiong, Y. Wu, Y. Liu, R. Ma, T. Sasaki, X. Wang and J. Zhu, Two-Dimensional Organic-Inorganic Superlattice-like Heterostructures for Energy Storage Applications, *Energy Environ. Sci.*, 2020, **13**, 4834–4853.
10 C. Liu, Q. Sun, L. Lin, J. Wang, C. Zhang, C. Xia, T. Bao, J. Wan, R. Huang, J. Zou and C. Yu, Ternary MOF-on-MOF Heterostructures with Controllable Architectural and Compositional Complexity via Multiple Selective Assembly, *Nat. Commun.*, 2020, **11**, 4971.
11 P. Geng, M. Du, C. Wu, T. Luo, Y. Zhang and H. Pang, PPy-constructed core-shell structure from MOFs for confining lithium polysulfides, *Inorg. Chem. Front.*, 2022, **9**, 2389–2394.
12 C. Gu, Y. Liu, B. Hu, Y. Liu, N. Zhou, L. Xia and Z. Zhang, Multicomponent Nanohybrids of Nickel/Ferric Oxides and Nickel Cobaltate Spinel Derived from the MOF-on-MOF Nanostructure as Efficient Scaffolds for Sensitively Determining Insulin, *Anal. Chim. Acta*, 2020, **1110**, 44–55.
13 W. Liu, L. Yu, R. Yin, X. Xu, J. Feng, X. Jiang, D. Zheng, X. Gao, X. Gao, W. Que, P. Ruan, F. Wu, W. Shi and X. Cao, Non-3d Metal Modulation of a 2D Ni–Co Heterostructure Array as Multifunctional Electrocatalyst for Portable Overall Water Splitting, *Small*, 2020, **16**, 1906775.
14 Y. Dai, C. Liu, Y. Bai, Q. Kong and H. Pang, Framework Materials for Supercapacitors, *Nanotechnol. Rev.*, 2022, **11**, 1005–1046.
15 D. Sheberla, J. C. Bachman, J. S. Elias, C. J. Sun, Y. Shao-Horn and M. Dincă, Conductive MOF Electrodes for Stable Supercapacitors with High Areal Capacitance, *Nat. Mater.*, 2017, **16**, 220–224.
16 S. Zheng, H. Zhou, H. Xue, P. Braunstein and H. Pang, Pillared-Layer Ni-MOF Nanosheets Anchored on Ti3C2 MXene for Enhanced Electrochemical Energy Storage, *J. Colloid Interface Sci.*, 2022, **614**, 130–137.
17 D. Zheng, H. Wen, X. Sun, X. Guan, J. Zhang, W. Tian, H. Feng, H. Wang and Y. Yao, Ultrathin Mn Doped Ni-MOF Nanosheet Array for Highly Capacitive and Stable Asymmetric Supercapacitor, *Chem. – Eur. J.*, 2020, **26**, 17149–17155.
18 X. Hang, J. Zhao, Y. Xue, R. Yang and H. Pang, Synergistic Effect of Co/Ni Bimetallic Metal–Organic Nanostructures for Enhanced Electrochemical Energy Storage, *J. Colloid Interface Sci.*, 2022, **628**, 389–396.
19 L. Jin and H. Pang, CoP @ SiO2 Nanoreactors: A Core-Shell Structure for Efficient Electrocatalytic Oxygen Evolution Reaction, *Chin. Chem. Lett.*, 2020, **31**, 2300–2304.
20 V. Ganesan, J. Son and J. Kim, CoP2/Fe-CoP2 Yolk – Shell Nanoboxes as Efficient Electrocatalysts for the Oxygen Evolution Reaction, *Nanoscale*, 2021, 4569–4575.
21 Y. Liu, H. Huang, L. Xue, J. Sun, X. Wang, P. Xiong and J. Zhu, Recent Advances in the Heteroatom Doping of Perovskite Oxides for Efficient Electrocatalytic Reactions, *Nanoscale*, 2021, **13**, 19840–19856.
22 J. Guo, Y. Wan, Y. Zhu, M. Zhao and Z. Tang, Advanced Photocatalysts Based on Metal Nanoparticle/Metal-Organic Framework Composites, *Nano Res.*, 2021, **14**, 2037–2052.
23 D. H. Hong, H. S. Shim, J. Ha and H. R. Moon, MOF-on-MOF Architectures: Applications in Separation, Catalysis, and Sensing, *Bull. Korean Chem. Soc.*, 2021, **42**, 956–969.
24 C. Liu, J. Wang, J. Wan and C. Yu, MOF-on-MOF Hybrids: Synthesis and Applications, *Coord. Chem. Rev.*, 2021, **432**, 213743.
25 K. Ikigaki, K. Okada, Y. Tokudome, T. Toyao, P. Falcaro, C. J. Doonan and M. Takahashi, MOF-on-MOF: Oriented Growth of Multiple Layered Thin Films of Metal–Organic Frameworks, *Angew. Chem., Int. Ed.*, 2019, **58**, 6886–6890.
26 T. Zhao, D. Wang, C. Cheng, D. Zhong, G. Hao, G. Liu, J. Li and Q. Zhao, Preparation of a Dual-MOF Heterostructure (ZIF@MIL) for Enhanced Oxygen Evolution Reaction Activity, *Chem. – Asian J.*, 2021, **16**, 64–71.
27 J. Yang, F. Zhang, H. Lu, X. Hong, H. Jiang, Y. Wu and Y. Li, Hollow Zn/Co ZIF Particles Derived from Core-Shell ZIF-67@ZIF-8 as Selective Catalyst for the Semi-Hydrogenation of Acetylene, *Angew. Chem., Int. Ed.*, 2015, **54**, 10889–10893.
28 H. Jia, A. Du, H. Zhang, J. Yang, R. Jiang, J. Wang and C. Y. Zhang, Site-Selective Growth of Crystalline Ceria with Oxygen Vacancies on Gold Nanocrystals for Near-Infrared Nitrogen Photofixation, *J. Am. Chem. Soc.*, 2019, **141**, 5083–5086.
29 C. Chen, D. Xiong, M. Gu, C. Lu, F. Y. Yi and X. Ma, MOF-Derived Bimetallic CoFe-PBA Composites as Highly Selective and Sensitive Electrochemical Sensors for Hydrogen Peroxide and Nonenzymatic Glucose in Human Serum, *ACS Appl. Mater. Interfaces*, 2020, **12**, 35365–35374.
30 X. Wu, Y. Ru, Y. Bai, G. Zhang, Y. Shi and H. Pang, PBA Composites and Their Derivatives in Energy and Environmental Applications, *Coord. Chem. Rev.*, 2022, **451**, 214260.
31 Z. Wu, Y. Wang, Z. Xiong, Z. Ao, S. Pu, G. Yao and B. Lai, Core-Shell Magnetic Fe3O4@Zn/Co-ZIFs to Activate Peroxymonosulfate for Highly Efficient Degradation of Carbamazepine, *Appl. Catal., B*, 2020, **277**, 119136.
32 J. Yan, Y. Huang, X. Han, X. Gao and P. Liu, Metal Organic Framework (ZIF-67)-Derived Hollow CoS2/N-Doped Carbon Nanotube Composites for Extraordinary Electromagnetic Wave Absorption, *Composites, Part B*, 2019, **163**, 67–76.
33 J. Nai, X. Wen and D. Lou, Hollow Structures Based on Prussian Blue and Its Analogs for Electrochemical Energy Storage and Conversion, *Adv. Mater.*, 2019, **31**, 1706825.
34 W. Shi, X. Liu, T. Deng, S. Huang, M. Ding, X. Miao, C. Zhu, Y. Zhu, W. Liu, F. Wu, C. Gao, S. W. Yang,

H. Y. Yang, J. Shen and X. Cao, Enabling Superior Sodium Capture for Efficient Water Desalination by a Tubular Polyaniline Decorated with Prussian Blue Nanocrystals, *Adv. Mater.*, 2020, **32**, 1907404.

35 X. Gu, Z. Liu, H. Liu, C. Pei and L. Feng, Fluorination of ZIF-67 Framework Templated Prussian Blue Analogue Nano-Box for Efficient Electrochemical Oxygen Evolution Reaction, *Chem. Eng. J.*, 2021, **403**, 126371.

36 R. Zhu, J. Ding, J. Yang, H. Pang, Q. Xu, D. Zhang and P. Braunstein, Quasi-ZIF-67 for Boosted Oxygen Evolution Reaction Catalytic Activity via a Low Temperature Calcination, *ACS Appl. Mater. Interfaces*, 2020, **12**, 25037–25041.

37 S. Cui, Y. He and X. Bo, Prussian Blue/ZIF-67-Derived Carbon Layers-Encapsulated FeCo Nanoparticles for Hydrogen and Oxygen Evolution Reaction, *J. Electroanal. Chem.*, 2019, **853**, 113557.

38 S. Ai, X. Guo, L. Zhao, D. Yang and H. Ding, Zeolitic Imidazolate Framework-Supported Prussian Blue Analogues as an Efficient Fenton-like Catalyst for Activation of Peroxymonosulfate, *Colloids Surf., A*, 2019, **581**, 123796.

39 K. Xu, C. Zhan, W. Zhao, X. Yu, Q. Zhu and L. Yang, J., Tunable Resistance of MOFs Films via an Anion Exchange Strategy for Advanced Gas Sensing, *Hazard. Mater.*, 2021, **416**, 125906.

40 S. Sutarsis, J. Patra, C. Y. Su, J. Li, D. Bresser, S. Passerini and J. K. Chang, Manipulation of Nitrogen-Heteroatom Configuration for Enhanced Charge-Storage Performance and Reliability of Nanoporous Carbon Electrodes, *ACS Appl. Mater. Interfaces*, 2020, **12**, 32797–32805.

41 C. Liu, Y. Bai, W. Li, F. Yang, G. Zhang and H. Pang, In Situ Growth of Three-Dimensional MXene/Metal–Organic Framework Composites for High-Performance Supercapacitors, *Angew. Chem., Int. Ed.*, 2022, **61**, e202116282.

42 Y. Bai, C. Liu, T. Chen, W. Li, S. Zheng, Y. Pi, Y. Luo and H. Pang, MXene-Copper/Cobalt Hybrids via Lewis Acidic Molten Salts Etching for High Performance Symmetric Supercapacitors, *Angew. Chem., Int. Ed.*, 2021, **60**, 25318–25322.

43 Y. Wang, Y. Liu, H. Wang, W. Liu, Y. Li, J. Zhang, H. Hou and J. Yang, Ultrathin NiCo-MOF Nanosheets for High-Performance Supercapacitor Electrodes, *ACS Appl. Energy Mater.*, 2019, **2**, 2063–2071.

44 C. Zhang, Q. Wang, W. Zhang, X. Li, Z. Zhu, C. Zhang, A. Xie and S. Luo, Preparation and Application of Co3O4-Ni-MOF/MWCNTs Hybrid for Supercapacitor, *Ionics*, 2021, **27**, 3543–3551.

45 Q. Jing, W. Li, J. Wang, X. Chen and H. Pang, Calcination Activation of Three-Dimensional Cobalt Organic Phosphate Nanoflake Assemblies for Supercapacitors, *Inorg. Chem. Front.*, 2021, **8**, 4222–4229.

